

NLO Corrections to Double Higgs Production in the Higgs Singlet Model

S. Dawson^a and I. M. Lewis^b

^a*Department of Physics, Brookhaven National Laboratory, Upton, N.Y., 11973, U.S.A.*

^b*SLAC National Accelerator Laboratory, 2575 Sand Hill Rd, Menlo Park, CA, 94025, U.S.A.*

(Dated: November 7, 2018)

Abstract

Higgs pair production at the LHC from gluon fusion is small in the Standard Model, but can be enhanced in models where a resonant enhancement is allowed. We examine the effect of a resonant contribution from a second scalar arising in a model with a gauge singlet scalar field in addition to the usual $SU(2)$ scalar doublet, with mass up to $M_H \sim 600 \text{ GeV}$ and discuss the interference effects in double Higgs production. The interference effects distort the double Higgs invariant mass distributions, and, depending on M_H , can enhance the total cross section by up to $\sim 20\%$ or decrease by $\sim 30\%$ for viable mixing parameters. We compute the NLO QCD corrections in the large m_t limit. The corrections are large and can also significantly distort kinematic distributions near the resonance peak.

I. INTRODUCTION

The experimental exploration of the Higgs sector of the Standard Model (SM) is one of the main goals of the current LHC run. Current data on Higgs properties are in reasonable agreement with the theoretical expectations, although there is still considerable room for new physics. An attractive extension of the SM is the Higgs portal scenario, in which the SM Higgs boson couples to a gauge singlet scalar, S , which in turn can communicate with a hidden sector. Models with an additional scalar singlet have also been used to generate a strong first order electroweak phase transition[1–6].

In the Higgs singlet model, the SM Higgs doublet mixes with the new singlet, S , to form two physical scalar bosons: one, h , identified with the observed $m_h = 125 \text{ GeV}$ resonance and a second, H , with mass M_H . When $M_H \gtrsim 2m_h$, large resonant enhancements are possible in double Higgs production from gluon fusion, significantly enhancing the rate compared to the SM prediction. The singlet model has the advantage of depending on relatively few parameters, allowing for straightforward experimental study at the LHC in the analysis of Higgs couplings[7], searches for heavy SM-like Higgs bosons[8–10] and direct searches for resonant di-Higgs production[11–14]. Higgs singlet models have also been extensively studied theoretically and additional limits derived from precision electroweak data, the interpretation of LHC results, and restrictions from the requirements of perturbative unitarity and perturbativity of the couplings[3, 15–30].

Double Higgs production from gluon fusion in the SM results from both triangle and box loop contributions, which interfere destructively, causing a suppression of the total rate from the naive estimate[31, 32]. This process has been studied at lowest order QCD (LO) in the singlet model, and regions of parameter space with enhanced rates determined. In this work, we consider precision predictions at NLO QCD for double Higgs production in the singlet model, including the hh invariant mass distribution. Since double Higgs production from gluon fusion first occurs at one-loop, the full NLO corrections involve two-loop virtual diagrams with massive internal particles. The calculation is considerably simplified by using an effective theory corresponding to the $m_t \rightarrow \infty$ limit of the SM. In the SM, the corrections to the total rate have been known at NLO for some time in the effective theory[33], which has also been matched onto the NNLL threshold resummed result [34]. Recently the rate has been calculated at NNLO[35, 36] and matched to the NNLL result[37]. These corrections

typically increase the rate by a factor of about 2 – 2.3. The SM NLO QCD corrections to $gg \rightarrow hh$ are also known in an effective field theory limit where the exact mass dependence is retained everywhere except in the virtual corrections[38] and alternatively in an expansion in $\frac{1}{m_t^{2n}}$ [39, 40]. The unknown m_t dependence of the higher order QCD corrections induces an uncertainty of $\mathcal{O}(\pm 10\%)$ in the SM predictions.

Higher order QCD corrections to new physics scenarios with resonant enhancements of the double Higgs rates have been derived for the MSSM[33, 41] and the two Higgs doublet model[42], and also in an effective operator formalism with no resonance[43]. These corrections not only affect the total rate, but in some regions of parameter space distort the shape of the distributions. In this paper, we examine the approximations behind the QCD corrections in the context of the Higgs singlet model. We demonstrate that the corrections in the resonance region are significant and that the use of a constant K factor is a poor approximation in this regime. We also investigate the interference effects between the heavy scalar and SM-like contributions. These effects can be significant and should be included in searches for new heavy scalars.

II. MODEL

A. Recap

We consider a simple extension of the SM containing the SM Higgs doublet, Φ , and an additional real gauge singlet scalar, S . After imposing a Z_2 symmetry under which $S \rightarrow -S$, the most general scalar potential is[15, 17]

$$V = -\mu^2 \Phi^\dagger \Phi - m^2 S^2 + \lambda (\Phi^\dagger \Phi)^2 + \frac{a_2}{2} \Phi^\dagger \Phi S^2 + \frac{b_4}{4} S^4. \quad (1)$$

Although not necessary for a strong first order electroweak phase transition, models without a Z_2 symmetry have been constructed in the context of electroweak baryogenesis[1–6]. However, the additional complication is not necessary for our discussion of higher order corrections. After spontaneous symmetry breaking, in the unitary gauge we have $\Phi^T = (0, \phi_0)/\sqrt{2}$ with $\langle \phi_0 \rangle \equiv v = 246 \text{ GeV}$ and $S \equiv (s + x)/\sqrt{2}$ with $\langle S \rangle = x/\sqrt{2}$.

The mass eigenstate fields, h and H , are:

$$\begin{pmatrix} h \\ H \end{pmatrix} = \begin{pmatrix} \cos \theta & -\sin \theta \\ \sin \theta & \cos \theta \end{pmatrix} \begin{pmatrix} \phi_0 - v \\ s \end{pmatrix}, \quad (2)$$

with physical masses, m_h and M_H , and $-\frac{\pi}{2} \leq \theta \leq \frac{\pi}{2}$.

The terms in the potential can be written in terms of the physical masses and mixing angle as,

$$\mu^2 = v^2 \lambda + \frac{1}{4} x^2 a_2 \quad (3)$$

$$m^2 = \frac{1}{4} (x^2 b_4 + v^2 a_2) \quad (4)$$

$$\lambda = \frac{m_h^2}{2v^2} + \frac{M_H^2 - m_h^2}{2v^2} \sin^2 \theta \quad (5)$$

$$a_2 = \frac{M_H^2 - m_h^2}{vx} (2 \sin \theta \cos \theta) \quad (6)$$

$$b_4 = \frac{2M_H^2}{x^2} + \frac{2(m_h^2 - M_H^2)}{x^2} \sin^2 \theta. \quad (7)$$

The requirement that the potential be bounded from below imposes,

$$a_2 > -2\sqrt{b_4 \lambda}, \quad \lambda, b_4 > 0. \quad (8)$$

We will also need the triple scalar couplings:

$$L \sim \frac{\lambda_{111}}{6} h^3 + \frac{\lambda_{211}}{2} H h^2 + \dots \quad (9)$$

where

$$\lambda_{111} = -\frac{3m_h^2}{v} \left(\cos^3 \theta - \tan \beta \sin^3 \theta \right) \quad (10)$$

$$\lambda_{211} = -\frac{m_h^2}{v} \sin 2\theta (\cos \theta + \sin \theta \tan \beta) \left(1 + \frac{M_H^2}{2m_h^2} \right) \quad (11)$$

and $\tan \beta \equiv \frac{v}{x}$. A complete list of the scalar self-couplings can be found in the Appendix of Ref. [19].

We assume that the lightest scalar, h , is the SM-like Higgs particle with $m_h = 125 \text{ GeV}$. The decay widths to SM particles, X , are then simply the SM values rescaled by the scalar mixing angle,

$$\begin{aligned} \Gamma(h \rightarrow X X^\dagger) &= \cos^2 \theta \Gamma(h \rightarrow X X^\dagger)_{SM} \\ \Gamma(H \rightarrow X X^\dagger) &= \sin^2 \theta \Gamma(H \rightarrow X X^\dagger)_{SM} \end{aligned} \quad (12)$$

where $\Gamma(H \rightarrow X X^\dagger)_{SM}$ is the SM partial width evaluated at mass M_H . The total widths are

$$\begin{aligned} \Gamma_h &= \cos^2 \theta \Gamma_h^{SM} \\ \Gamma_H &= \sin^2 \theta \Gamma_H^{SM} + \theta (M_H - 2m_H) \Gamma(H \rightarrow hh), \end{aligned} \quad (13)$$

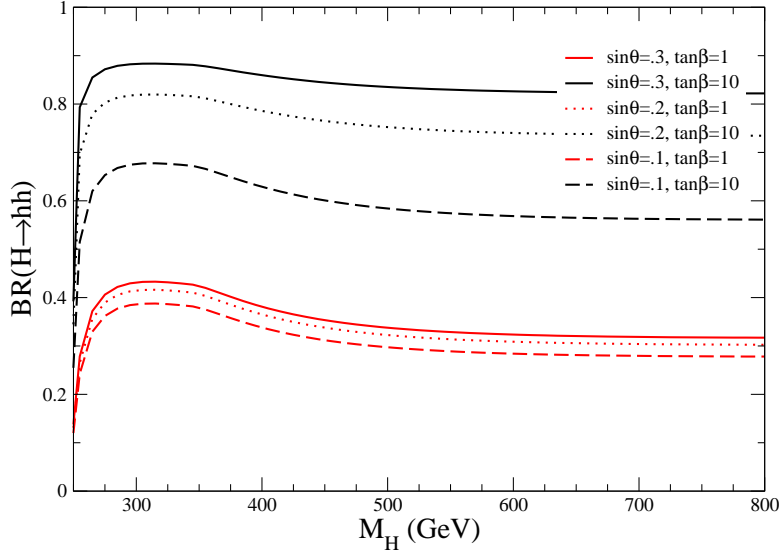


FIG. 1: Branching ratio for $H \rightarrow hh$.

where Γ_H^{SM} is the SM total width evaluated at mass M_H and

$$\Gamma(H \rightarrow hh) = \frac{\lambda_{211}^2}{32\pi M_H} \sqrt{1 - \frac{4m_h^2}{M_H^2}}. \quad (14)$$

The branching ratio of $H \rightarrow hh$ is shown in Fig. 1. For small $\sin\theta$, the branching ratio is relatively insensitive to $\tan\beta$ and is approximately $\text{BR}(H \rightarrow hh) \sim 0.3 - 0.4$.

The model has 5 free parameters which we take to be:

$$m_h = 125 \text{ GeV}, M_H, v = 246 \text{ GeV}, \tan\beta, \cos\theta. \quad (15)$$

B. Limits

The Z_2 symmetric Higgs singlet model is restricted by a number of experimental measurements. Fits to the h couplings assuming no branching ratio to invisible particles require $|\cos\theta| > 0.93$ at 95% confidence level[7]. Precision electroweak quantities[44], in particular the W boson mass[45], receive contributions which are sensitive to M_H and $\cos\theta$. For $M_H \gtrsim 400 \text{ GeV}$, measurements of the W mass require $|\cos\theta| > 0.96$, with the limits significantly weaker for smaller M_H [15, 20]. Heavy Higgs searches can also be interpreted as limits on $\cos\theta$. For $M_H \lesssim 300 \text{ GeV}$, these limits are stronger than the limits from the W mass. Assuming no branching ratio, $H \rightarrow hh$, the direct search limits for heavy Higgs bosons can be interpreted as requiring $|\cos\theta| > 0.92$ in this region. Requiring b_4 to remain perturbative

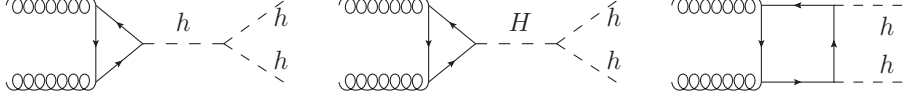


FIG. 2: Feynman diagrams contributing to $gg \rightarrow hh$ in the singlet model.

as it is scaled to high energy gives an upper limit on $\tan \beta$ which depends on M_H and θ : for $\sin \theta = 0.1$ and $M_H = 200(500) \text{ GeV}$, $\tan \beta < 1.5(0.5)$ [16, 20]. With these considerations in mind, we will in general present results with $\cos \theta = 0.96$, $\tan \beta = 0.5$.

III. DOUBLE HIGGS PRODUCTION

A. LO Results

Two Higgs production arises from the Feynman diagrams shown in Fig. 2. The result is sensitive to new colored objects with mass m (fermions or scalars) in the loops [46–51] and also to the 3– Higgs self-couplings. The amplitude for $g^{A,\mu}(p)g^{B,\nu}(q) \rightarrow h(p')h(q')$ can be written as,

$$A_{AB}^{\mu\nu} = \frac{\alpha_s}{8\pi v^2} \delta_{AB} \left(P_1^{\mu\nu}(p, q) F_1(s, t, u, m^2) + P_2^{\mu\nu}(p, q, p') F_2(s, t, u, m^2) \right), \quad (16)$$

where P_1 and P_2 are the orthogonal projections onto the spin-0 and spin-2 states respectively,

$$P_1^{\mu\nu}(p, q) = g^{\mu\nu} - \frac{p^\nu q^\mu}{p \cdot q}$$

$$P_2^{\mu\nu}(p, q, p') = g^{\mu\nu} + \frac{2}{sp_T^2} \left\{ m_h^2 p^\nu q^\mu + (t - m_h^2) q^\mu p'^\nu + (u - m_h^2) p^\nu p'^\mu + sp'^\mu p'^\nu \right\}, \quad (17)$$

s, t , and u are the partonic Mandelstam variables,

$$s = (p + q)^2$$

$$t = (p - p')^2$$

$$u = (p - q')^2$$

$$p_T^2 = \left(\frac{ut - m_h^4}{s} \right). \quad (18)$$

The functions F_1 and F_2 are known analytically[31, 32] and the partonic cross section is given in terms of the form factors by,

$$\frac{d\hat{\sigma}_{LO}^{m_t}}{dt} = \frac{\alpha_s^2(\mu_R)}{2^{15}\pi^3 v^4} \left(\frac{|F_1(s, t, u, m_t^2)|^2 + |F_2(s, t, u, m_t^2)|^2}{s^2} \right), \quad (19)$$

where μ_R is the renormalization scale. (We have included the factor of $\frac{1}{2}$ for identical particles in the final state). In the singlet model (as in the SM), the dominant contribution comes from top quark loops. The form factors can be written as,

$$\begin{aligned}
F_1(s, t, u, m_t^2) &\equiv F_1^{tri}(s, t, u, m_t^2) + F_1^{box}(s, t, u, m_t^2) \\
F_1^{tri}(s, t, u, m_t^2) &= -s \left(\frac{\cos \theta \lambda_{111} v}{s - m_h^2 + i m_h \Gamma_h} + \frac{\sin \theta \lambda_{211} v}{s - M_H^2 + i M_H \Gamma_H} \right) F_\Delta(s, m_t^2) \\
F_1^{box}(s, t, u, m_t^2) &= s \cos^2 \theta F_\square(s, t, u, m_t^2) \\
F_2(s, t, u, m_t^2) &= s \cos^2 \theta G_\square(s, t, u, m_t^2).
\end{aligned} \tag{20}$$

In the limit $m_t \rightarrow \infty$,

$$\begin{aligned}
F_\Delta &\rightarrow \frac{4}{3} \\
F_\square &\rightarrow -\frac{4}{3} \\
G_\square &\rightarrow 0.
\end{aligned} \tag{21}$$

The form factors F_Δ , F_\square , and G_\square including the full kinematic dependences are found in Refs. [31, 32]¹. We denote the cross section found by including the exact m_t dependence of the matrix elements, Eq. 20, by $\hat{\sigma}_{LO}^{m_t}$, and the $m_t \rightarrow \infty$ limit, Eq. 21, as $\hat{\sigma}_{LO}^{m_t \rightarrow \infty}$.

The LO hadronic cross section is,

$$\sigma_{LO}^{m_t} = \int_{\tau_0}^1 d\tau \frac{d\mathcal{L}^{gg}}{d\tau} \hat{\sigma}_{LO}^{m_t}(s = \tau S), \tag{22}$$

and the luminosity function is defined,

$$\frac{d\mathcal{L}^{ij}}{d\tau} = \sum_{ij} \int_\tau^1 \frac{dx}{x} f_i(x, \mu_F) f_j\left(\frac{\tau}{x}, \mu_F\right), \tag{23}$$

S is the square of the hadronic energy, $\tau_0 = \frac{4m_h^2}{S}$, and μ_F is the factorization scale.

B. NLO Corrections

The NLO corrections in the SM are known in the large m_t limit[33] and are trivially generalized to the singlet model. The gg initial state contains IR singularities which cancel

¹ The functions defined in Eq. 20 satisfy $F_\Delta(F_\square, G_\square) \rightarrow 2F_\Delta(F_\square, G_\square)$ (Ref. [31]) and $sF_\Delta(sF_\square, sG_\square) \rightarrow F_\Delta(F_\square, G_\square)$ (Ref. [32]).

when the real and virtual contributions are combined. The remaining collinear divergences in the gg , qg and $q\bar{q}$ initial states are absorbed into the NLO PDFs defined in the \overline{MS} scheme with 5 light flavors. The terms listed below are the finite contributions obtained after canceling the singularities. We write the NLO rate as,

$$\sigma_{\text{NLO}}^{m_t}(pp \rightarrow hh) = \sigma_{\text{LO}}^{m_t} + \sigma_{\text{virt}}^{m_t} + \sigma_{gg}^{m_t} + \sigma_{gq}^{m_t} + \sigma_{q\bar{q}}^{m_t}, \quad (24)$$

where,

$$\begin{aligned} \sigma_{\text{virt}}^{m_t} &= \frac{\alpha_s(\mu_R)}{\pi} \int_{\tau_0}^1 d\tau \frac{d\mathcal{L}^{gg}}{d\tau} \hat{\sigma}_{\text{LO}}^{m_t}(s = \tau S) C^{m_t}, \\ \sigma_{gg}^{m_t} &= \frac{\alpha_s(\mu_R)}{\pi} \int_{\tau_0}^1 d\tau \frac{d\mathcal{L}^{gg}}{d\tau} \int_{\tau_0/\tau}^1 \frac{dz}{z} \hat{\sigma}_{\text{LO}}^{m_t}(s = z\tau S) \left\{ -z P_{gg}(z) \log \frac{\mu_F^2}{\tau S} \right. \\ &\quad \left. - \frac{11}{2}(1-z)^3 + 6[1+z^4 + (1-z)^4] \left(\frac{\log(1-z)}{1-z} \right)_+ \right\}, \\ \sigma_{gq}^{m_t} &= \frac{\alpha_s(\mu_R)}{\pi} \int_{\tau_0}^1 d\tau \sum_{q,\bar{q}} \frac{d\mathcal{L}^{gq}}{d\tau} \int_{\tau_0/\tau}^1 \frac{dz}{z} \hat{\sigma}_{\text{LO}}^{m_t}(s = z\tau S) \left\{ -\frac{z}{2} P_{gq}(z) \log \frac{\mu_F^2}{\tau S(1-z)^2} \right. \\ &\quad \left. + \frac{2}{3} z^2 - (1-z)^2 \right\}, \\ \sigma_{q\bar{q}}^{m_t} &= \frac{\alpha_s(\mu_R)}{\pi} \int_{\tau_0}^1 d\tau \sum_q \frac{d\mathcal{L}^{q\bar{q}}}{d\tau} \int_{\tau_0/\tau}^1 \frac{dz}{z} \hat{\sigma}_{\text{LO}}^{m_t}(s = z\tau S) \frac{32}{27} (1-z)^3. \end{aligned} \quad (25)$$

We follow the philosophy of Ref. [33] and approximate the form factors in the virtual corrections by the exact m_t dependent quantities and include the full mass dependence in $\hat{\sigma}_{\text{LO}}^{m_t}$ in Eq. 25. The coefficient, C^{m_t} , for the virtual corrections is

$$\begin{aligned} C^{m_t} &= \pi^2 + \frac{11}{2} + \frac{33 - 2n_{lf}}{6} \log \frac{\mu_R^2}{s} \\ &\quad + \frac{8s}{9} \cos^2 \theta \text{Real} \left(\frac{\int_{-\frac{s}{4}(\beta+1)^2}^{-\frac{s}{4}(\beta-1)^2} dt \left\{ F_1(s, t, u, m_t^2) - \frac{p_T^2}{2tu} (s - 2m_h^2) F_2(s, t, u, m_t^2) \right\}}{\int_{-\frac{s}{4}(\beta+1)^2}^{-\frac{s}{4}(\beta-1)^2} dt \left\{ |F_1(s, t, u, m_t^2)|^2 + |F_2(s, t, u, m_t^2)|^2 \right\}} \right) \end{aligned} \quad (26)$$

and

$$\beta \equiv \sqrt{1 - \frac{4m_h^2}{s}}. \quad (27)$$

$P_{gg}(z)$ and $P_{gq}(z)$ are the DGLAP splitting functions,

$$\begin{aligned} P_{gg}(z) &= 6 \left\{ \left(\frac{1}{1-z} \right)_+ + \frac{1}{z} - 2 + z(1-z) \right\} + \frac{33 - 2n_{lf}}{6} \delta(1-z), \\ P_{gq}(z) &= \frac{4}{3} \frac{1 + (1-z)^2}{z}, \end{aligned} \quad (28)$$

where $n_{lf} = 5$. The result in Eq. 25 has only approximate finite m_t dependence since it has been adapted from the NLO calculation in the $m_t \rightarrow \infty$ limit [33].

We define an m_t dependent differential K factor from Eqs. 22 and 25,

$$K^{m_t} \equiv \frac{d\sigma_{NLO}^{m_t}}{dM_{hh}} \bigg/ \frac{d\sigma_{LO}^{m_t}}{dM_{hh}}, \quad (29)$$

where M_{hh} is the invariant mass of the final state double Higgs system. In the following section, we will also show the numerical effects on the K factor of replacing the form factors and LO cross section by their $m_t \rightarrow \infty$ limits,

$$K^{m_t \rightarrow \infty} \equiv \frac{d\sigma_{NLO}^{m_t \rightarrow \infty}}{dM_{hh}} \bigg/ \frac{d\sigma_{LO}^{m_t \rightarrow \infty}}{dM_{hh}}, \quad (30)$$

where,

$$C^{m_t \rightarrow \infty} = \pi^2 + \frac{11}{2} + \frac{33 - 2n_{lf}}{6} \log \frac{\mu_R^2}{s} + \frac{2}{3} \cos^2 \theta \frac{\text{Real} \left(c_\Delta(s) - \cos^2 \theta \right)}{|c_\Delta(s) - \cos^2 \theta|^2} \quad (31)$$

and

$$c_\Delta = \left(\frac{\cos \theta \lambda_{111} v}{s - m_h^2 + i m_h \Gamma_h} + \frac{\sin \theta \lambda_{211} v}{s - M_H^2 + i M_H \Gamma_H} \right). \quad (32)$$

IV. RESULTS

Our results are computed using CT12NLO PDFs[52] with a central scale choice $\mu_R = \mu_F \equiv \mu = M_{hh}$ for the renormalization and factorization scales, and with $m_t = 173.34 \text{ GeV}$ and $m_b = 4.62 \text{ GeV}$. In the computation of $\Gamma(H \rightarrow hh)$, we use the \overline{MS} NNLO running mass for $\overline{m}_b(M_H)$ and we always assume that $m_h = 125 \text{ GeV}$ is the lightest Higgs boson. Finally, the production cross section is computed including only the top quark loops, which are the largest contribution. Our numerical results in the SM are checked using the program HPAIR[33]. The singlet model results from our private code were checked by incorporating the resonance from the singlet model in HPAIR and comparing the two results.

A. SM Results

The LO rate for $gg \rightarrow hh$ in the SM is well known, as are the NLO and NNLO rates in the $m_t \rightarrow \infty$ limit. Ref. [37] finds the NNLO matched to NNLL rate of 36.8 fb for $pp \rightarrow hh$ at $\sqrt{S} = 13 \text{ TeV}$, $\mu = M_{hh}$, using MSTW2008 PDFs. The contributions to the differential

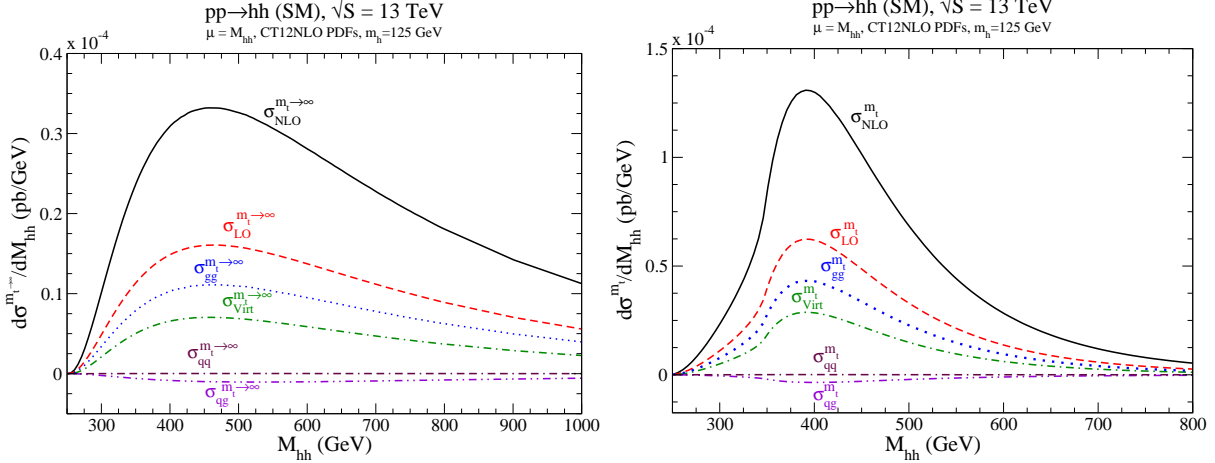


FIG. 3: Contributions to the SM rate for $pp \rightarrow hh$ at $\sqrt{S} = 13 \text{ TeV}$ in the $m_t \rightarrow \infty$ limit (LHS) and using the approximated m_t dependence of Eqs. 25,26 (RHS).

SM NLO cross section are shown in Fig. 3 in the $m_t \rightarrow \infty$ limit (LHS) and in the m_t dependent approximation of Eqs. 25 and 26 (RHS). The normalization and shapes of the 2 approximations are quite different, but the K factors computed from the 2 approximations are almost identical. The contributions from real gluon emission, σ_{gg} , and from the one-loop virtual diagrams, σ_{virt} , are of similar sizes, while the contributions from quark initial states are highly suppressed. In Fig. 4, we show the NLO result with approximate m_t dependence as defined in Eqs. 25, 26, and LO results for $m_t \rightarrow \infty$ and including the m_t dependence exactly. The lowest order result in the $m_t \rightarrow \infty$ limit overshoots the exact lowest order result at high M_{hh} and fails to reproduce the peak structure, as is well known. Including the NLO corrections significantly increases the rate. (Calculating $K^{m_t \rightarrow \infty}$ from the LHS of Fig. 3 and weighting by the exact m_t dependent LO result gives a curve which is almost indistinguishable from the NLO curve of Fig. 4.)

We show the renormalization/factorization scale variation of the SM LO and NLO rates in Fig. 5 when $M_{hh}/2 < \mu < 2M_{hh}$. In this figure, the LO rate includes all top mass dependence and the NLO rates are calculated using Eq. 25. The fractional scale dependence is significantly reduced at NLO. The scale variation of the differential SM K^{m_t} factor defined in Eq. 29 is shown in Fig. 6. At $M_{hh} = 400 \text{ GeV}$, the NLO scale uncertainty is $\sim 11\%$, while at $M_{hh} = 800 \text{ GeV}$ it is $\sim 15\%$. In the SM, the differential K factor is only slightly dependent on M_{hh} and can be accurately approximated by a constant.

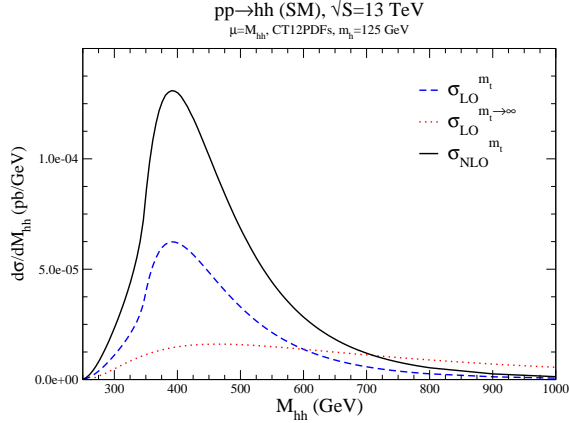


FIG. 4: SM differential cross section for $pp \rightarrow hh$ at $\sqrt{S} = 13 \text{ TeV}$. The NLO curve labelled σ^{mt} is obtained from Eqs. 25,26.

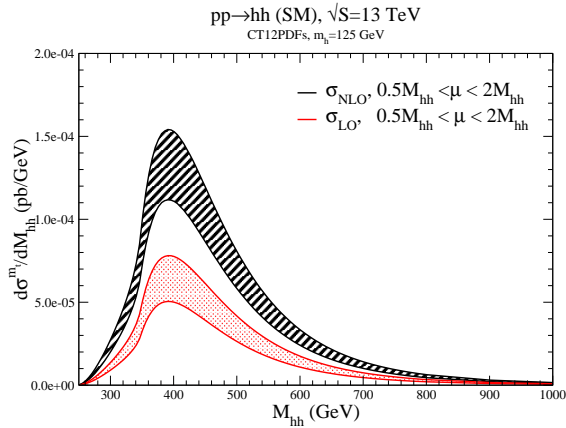


FIG. 5: Scale dependence of the SM differential cross section for $pp \rightarrow hh$ at $\sqrt{S} = 13 \text{ TeV}$. The NLO curves are obtained using Eqs. 25,26.

B. Singlet Model Results

We begin by showing some lowest order results. The LO rate as a function of M_H is shown in Figs. 7 and 8. For the smaller values of $\tan\beta$ and θ , the resonances become narrower, while for heavier M_H the height of the resonance peak and the dip above the peak due to interference effects become smaller. The strength of the destructive interference is particularly strong for $M_H = 200 \text{ GeV}$. Interference effects will be more thoroughly discussed in the next section, but we give an outline here. As in the SM, the box diagram dominates the h -resonance. Hence, the major contributions to interference are between the h - and H -resonances and the box diagram. The h -resonance and box diagrams (SM

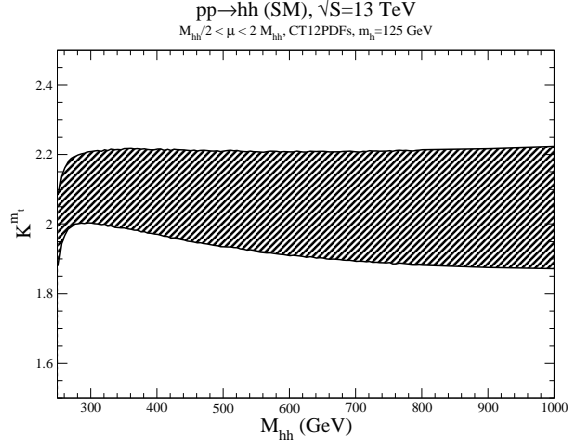


FIG. 6: Scale variation of the SM K^{mt} factor, Eq. 29, for $pp \rightarrow hh$ at $\sqrt{S} = 13 \text{ TeV}$ when the scale is varied $\frac{M_{hh}}{2} < \mu < 2M_{hh}$.

like contributions) have destructive interference, and the H -resonance and box diagrams have constructive (destructive) interference for $M_{hh} < M_H$ ($M_{hh} > M_H$). In the SM, the h -resonance and box diagrams have exact destructive interference at the double-Higgs threshold. In the singlet model the cancellation is not exact anymore due to changes in the tri-linear coupling and different mixing angle suppressions of the two diagrams, but the SM like contributions still have the strongest destructive interference at threshold. For $M_H < 2m_h$, both h - and H -resonance diagrams have strong destructive interference with the box diagram near $M_{hh} \sim 2m_h$. Hence, the overall destructive interference dip is strongest for $M_H = 200 \text{ GeV}$.

In picking a parameter point, we have a choice as to whether to choose a positive or negative sign for $\sin\theta$. The comparison of these two choices is shown in Fig. 8, with the LHS showing the differential cross sections and the RHS the ratio of total cross sections. As shown in the LHS of Fig. 8, the choice of sign makes little difference in the shape of the distributions. In particular, the interference effects remain essentially unchanged. This can be understood by analyzing the triple couplings λ_{111} (Eq. 10) and λ_{211} (Eq. 11), and F_1 (Eq. 20). The dependence of the cross section on the sign of $\sin\theta$ always appears with an associated factor of $\tan\beta$ and is suppressed compared to the $\cos\theta$ terms in the triple couplings. However, there can still be a significant change in the total rate, as shown on the RHS of Fig. 8. For $M_H > 2m_h$, the cross section for negative $\sin\theta$ is $\sim 70 - 80\%$ that of the cross section for positive $\sin\theta$. For $M_H < 2m_h$, the two cross sections are nearly the

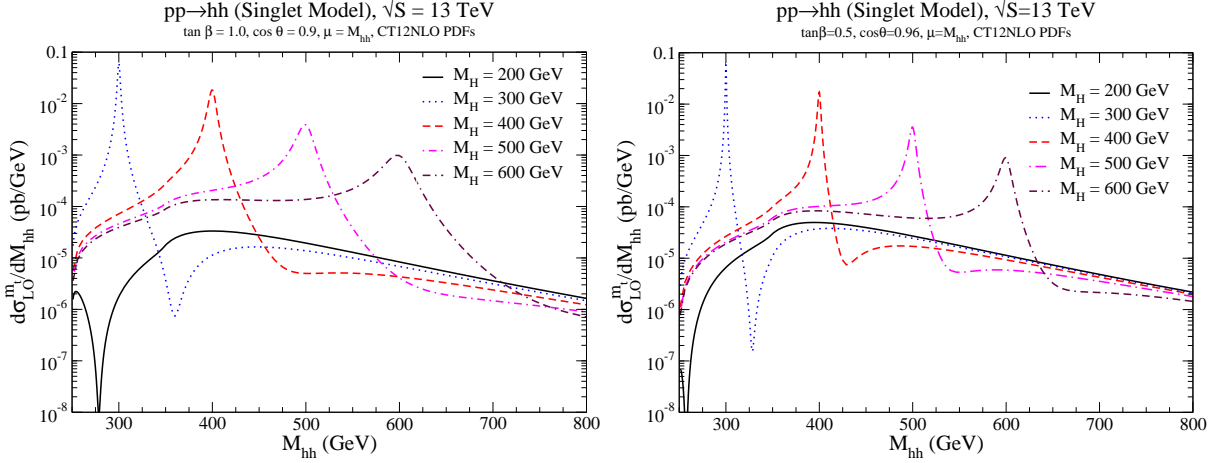


FIG. 7: Exact LO rates for $pp \rightarrow hh$ at $\sqrt{S} = 13 \text{ TeV}$ for fixed singlet mixing parameters, $\cos \theta = 0.9$ and $\tan \beta = 1.0$ (LHS) and $\cos \theta = 0.96$ and $\tan \beta = 0.5$ (RHS).

same. This can be understood, and is shown later, by noting that the H resonance makes a subleading contribution for $M_H < 2m_h$ GeV and the SM like contributions only depend on the sign of $\sin \theta$ in a highly suppressed $\sin^3 \theta$ term in λ_{111} . Throughout the rest of the paper we will choose a positive sign for $\sin \theta$.

In Fig. 9, we show the ratio of the singlet model rate normalized to the SM rate. It is clear that near the resonances large enhancements in the rates are possible and the singlet model should be clearly distinguishable from the SM.

C. Interference effects

The presence of the second scalar leads to interesting interference effects with the SM-like contributions. The real parts of the propagators in F_1^{tri} (Eq. 20) interfere destructively for $m_h < M_{hh} < M_H$ and constructively for $M_{hh} > M_H$, as is typical for the interference of two resonances². However, in the SM the box and triangle diagrams destructively interfere, with the box diagram dominating at large M_{hh} [55]. Hence, although the propagators of the two resonances destructively interfere, the H -propagator constructively interferes with the box diagram for $M_{hh} < M_H$, and destructively interferes for $M_{hh} > M_H$.

Leading order differential cross sections with individual contributions are shown sepa-

² This same interference effect is seen in the process $gg \rightarrow ZZ$ in the singlet model[53, 54] and in Drell-Yan production below the Z peak.

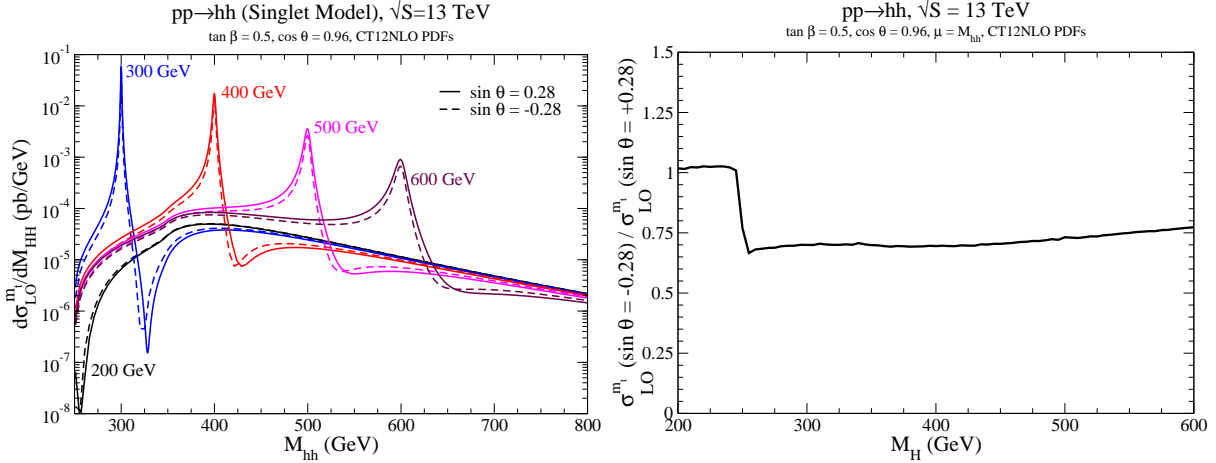


FIG. 8: Exact LO rates for $pp \rightarrow hh$ at $\sqrt{S} = 13 \text{ TeV}$ for fixed singlet mixing parameters $\cos \theta = 0.96$ and $\tan \beta = 0.5$. (LHS) The solid (dashed) curves correspond to choosing a positive (negative) sign for $\sin \theta$. (RHS) The ratio of the total LO cross sections with negative and positive sign for $\sin \theta$.

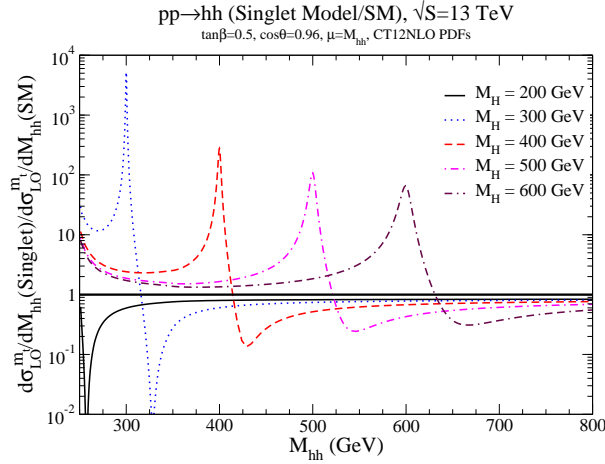


FIG. 9: Exact LO rates for $pp \rightarrow hh$ normalized to the exact LO SM rate at $\sqrt{S} = 13 \text{ TeV}$ for fixed singlet mixing parameters, $\cos \theta = 0.96$ and $\tan \beta = 0.5$.

rately in Figs. 10 and 11. The curves labelled “ $h + H$ resonances only” include the contributions of both s -channel h and H and their interference, but not the effect of the box diagrams. The destructive interference between the two propagators for $M_{hh} < M_H$ is clear. The curves labelled “no H -resonance” have the H resonance contribution removed; that is, only the SM-like contributions are included. As described above, by comparing the curves labelled “no H -resonance” with the total distribution, we see that there is constructive in-

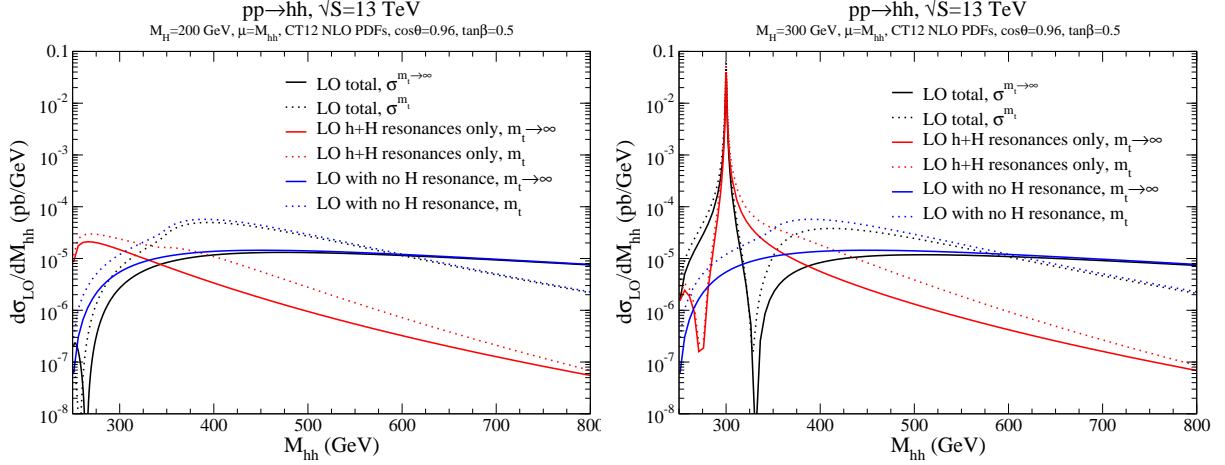


FIG. 10: LO results for $pp \rightarrow hh$ at $\sqrt{S} = 13 \text{ TeV}$ for $M_H = 200 \text{ GeV}$ (LHS) and $M_H = 300 \text{ GeV}$ (RHS), $\cos \theta = 0.96$ and $\tan \beta = 0.5$. See text for description of individual curves.

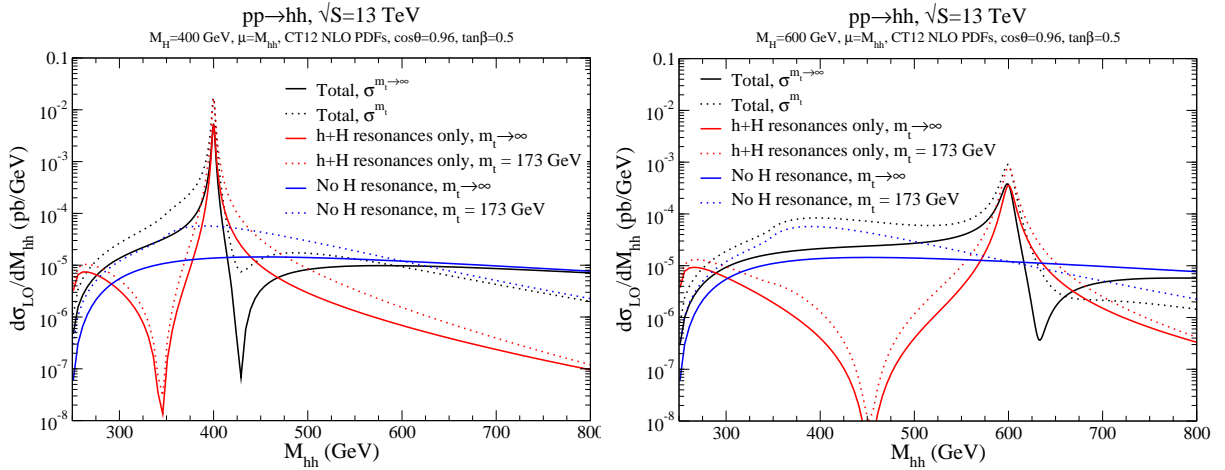


FIG. 11: LO results for $pp \rightarrow hh$ at $\sqrt{S} = 13 \text{ TeV}$ for $M_H = 400 \text{ GeV}$ (LHS), $M_H = 600 \text{ GeV}$ (RHS), with $\cos \theta = 0.96$ and $\tan \beta = 0.5$. See text for description of individual curves.

interference between the H and SM-like diagrams for $M_{hh} < M_H$ and destructive interference for $M_{hh} > M_H$. It is apparent that the $m_t \rightarrow \infty$ limit fails to reproduce the correct interference structure near and slightly above the peak and overshoots the rate at high M_{hh} . The location of the interference dip just above the resonance is slightly shifted to larger M_{hh} in the $m_t \rightarrow \infty$ limit. This motivates weighting the NLO rate (which is only known in the $m_t \rightarrow \infty$ limit), by the exact LO rate.

We show the ratio of the interference between the H resonance and SM-like diagrams and the full invariant mass distribution in Fig. 12. Exact m_t dependence has been kept. The

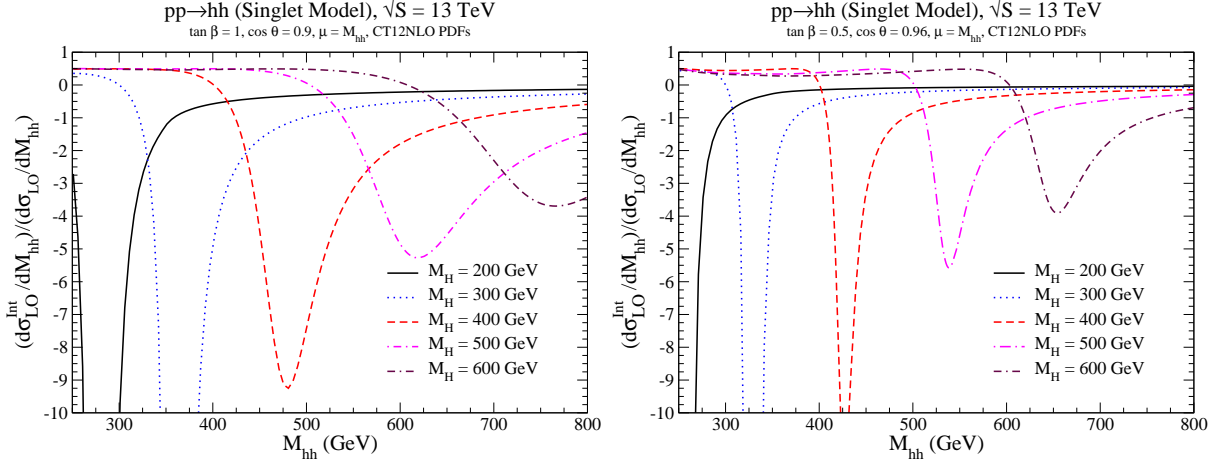


FIG. 12: Ratio of the interference between the H -resonance and the SM-like contributions, h -resonance+box, and the full invariant mass distribution with $\tan\beta = 1.0$ and $\cos\theta = 0.9$ (LHS), and $\tan\beta = 0.5$ and $\cos\theta = 0.96$ (RHS). The curves use the exact LO matrix elements.

interference contribution is

$$\frac{d\sigma_{LO}^{Int}}{dM_{hh}} = \frac{d\sigma_{LO}}{dM_{hh}} - \left(\frac{d\sigma_{LO}^H}{dM_{hh}} + \frac{d\sigma_{LO}^{h+Box}}{dM_{hh}} \right), \quad (33)$$

where σ^H contains only the contribution from the H -resonance, and σ^{h+Box} contains the h -resonance and box contributions and their interference. An interesting feature of Fig. 12 is that for $M_{hh} \ll M_H$, the interference contribution is independent of M_H for fixed θ and $\tan\beta$. This somewhat surprising effect can be understood by taking F_1 (Eq. 20) in the limit $m_h^2, s \ll M_H^2$:

$$F_1 \rightarrow -s \left(\frac{\cos\theta \lambda_{111} v}{s - m_h^2 + im_h \Gamma_h} + \frac{\sin\theta \sin 2\theta}{2} (\cos\theta + \sin\theta \tan\beta) \right) F_\Delta(s, m_t^2) + s \cos^2\theta F_\square(s, t, u, m_t^2). \quad (34)$$

As can be clearly seen, in this limit, the double Higgs rate does not explicitly depend on the heavy scalar mass.

The ratio of the interference between the H -resonance and SM-like contributions defined in Eq. 33 and the total cross section are shown in the LHS of Fig. 13. We also show the ratio of the H -resonance contribution only and the total cross section in the RHS of Fig. 13. The curves are shown for the two parameter points $\tan\beta = 1, \cos\theta = 0.9$ (solid black) and $\tan\beta = 0.5, \cos\theta = 0.96$ (dotted red). At amplitude level, the dominant (box) contribution to the SM-like pieces is proportional to $\cos^2\theta$ and makes a similar contribution

for both parameter points. However, below $2m_h$ the H -resonance amplitude is proportional to $\sin^2\theta$ and sensitive to relatively small changes in $\cos\theta$. This explains why for $M_H < 2m_h$ the interference and H -resonance contributions are larger for $\cos\theta = 0.9$ than for $\cos\theta = 0.96$. For $M_H > 2m_h$ and using the narrow-width-approximation, the H -resonance amplitude is proportional to $\sin\theta$ and is still larger for $\cos\theta = 0.9$ than for $\cos\theta = 0.96$. Once the resonance production of hh turns on, $M_H \sim 2m_h$, the H -resonance contribution dominates, as seen in the RHS of Fig. 13. As M_H increases, the H -propagator suppresses the H -resonance contribution. However, as M_H approaches $2m_t$, as is well-known in single Higgs production, the production rate through a top quark triangle increases. For $2m_h \lesssim M_H \lesssim 2m_t$ these two effects cancel each other and the contribution from the H -resonance is relatively constant. As M_H increases above $\sim 2m_t$, the suppression from the H -propagator is the dominant effect. Hence, the fractional contribution from the H -resonance only decreases and the fractional contribution from interference increases. These two effects are correlated because the SM-like contribution by itself is independent of M_H . It should be noted that the absolute contribution from the interference is nearly independent of M_H for $M_H \gtrsim 500$ GeV. This can be understood from Eq. 33. Since for increasing M_H there is a large contribution to the cross section from the $M_H \gg M_{hh}$ region, the total contribution to the interference is largely independent of M_H .

D. NLO Effects

In Fig. 14, we show the enhancement of the total cross section in the singlet model, relative to the SM rate. For $\tan\beta = 5$ and $\cos\theta = 0.96$, the maximum enhancement is of $\mathcal{O}(8)$ for $M_H \lesssim 500$ GeV and decreases rapidly to $\mathcal{O}(1)$ for larger M_H . For larger mixing, $\tan\beta = 1$ and $\cos\theta = 0.9$, enhancements of the SM rate up to a factor of ~ 22 are possible. We see that σ^{m_t}/σ_{SM} is not very different for LO and NLO total rates. The contribution of the H resonance in the narrow width approximation is accurate for $M_H \lesssim 400$ GeV, but underestimates the enhancement for larger M_H .

We now present our numerical results for the double Higgs invariant mass distributions at NLO. Fig. 15 shows the individual contributions (Eq. 25) to the invariant mass distributions using the approximation of Eqs. 25,26. It is important to remember that the full m_t dependent NLO rate is not known. We plot the absolute value of the qg contribution, since

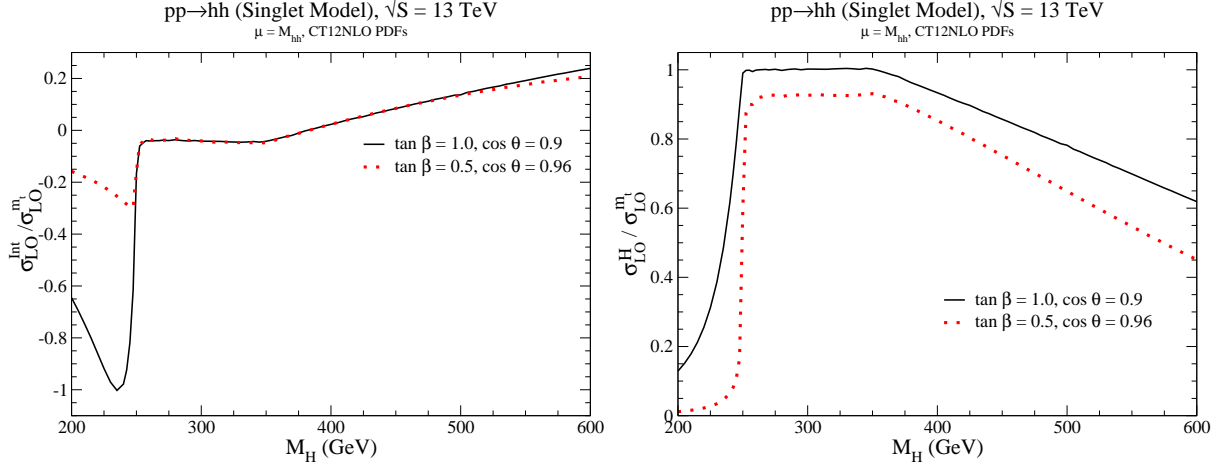


FIG. 13: Ratio of the interference between the H -resonance and the SM-like contributions, h -resonance+box, and the total cross section as a function of M_H (LHS). Ratio of the H-resonance contribution only and the total rate (RHS). Both $\tan \beta = 1.0, \cos \theta = 0.9$ (solid black) and $\tan \beta = 0.5, \cos \theta = 0.96$ (dotted red) are shown. The curves use the exact LO matrix elements.

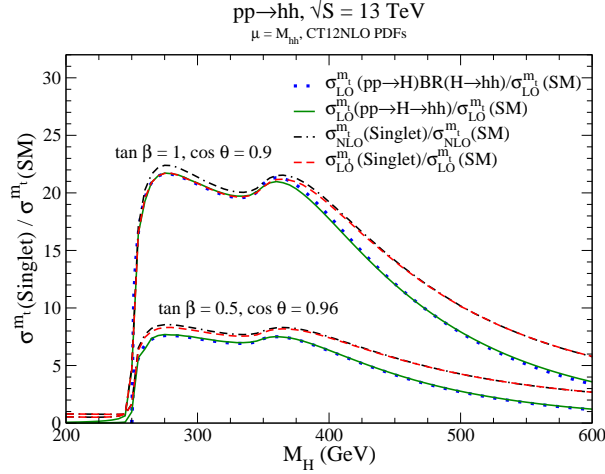


FIG. 14: Ratio of NLO (dash-dot black) and LO (dashed red) rates to the respective SM rates. Also, the ratio of the LO H-resonance only contribution calculated using the Breit-Wigner resonance (solid green) and in the narrow-width approximation (blue dotted) to the LO SM rate.

it is negative. The leading corrections are from the gg and virtual contributions, while the $q\bar{q}$ and $q\bar{q}$ contributions are subleading.

It is interesting to compare the effect of the approximations to the top mass dependence at NLO. In Fig. 16, we compare the NLO rate for $M_H = 300 \text{ GeV}$ computed using the approximation of Eqs. 25,26 (dashed red curve) with that obtained by computing $K^{m_t \rightarrow \infty}$

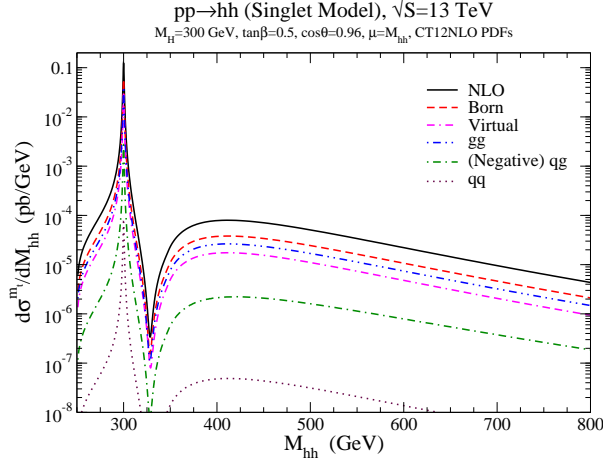


FIG. 15: Total and individual contributions to the NLO cross sections defined in Eqs. 25,26. The model parameters were chosen to be $\tan \beta = 0.5$, $\cos \theta = 0.96$, and $M_H = 300 \text{ GeV}$.

(Eq. 30) and weighting by the exact m_t dependent LO cross section (solid black). The curves overlap almost exactly. Since most contributions to the NLO rate (Eq. 25) are proportional to the LO rate, the approximate m_t dependence is mostly captured by weighting the exact LO rate with $K^{m_t \rightarrow \infty}$. The only complication is a piece of the virtual contribution (Eq. 26) that is not proportional to the LO rate. However, this piece turns out to make a small contribution.

We then compare with an NLO rate computed in the $m_t \rightarrow \infty$ limit (dotted blue in Fig. 16), i.e. this result is not reweighted by the exact m_t dependent LO result. The $m_t \rightarrow \infty$ limit shifts the location of the interference dip to slightly higher M_{hh} . This effect is also apparent in the comparison of the exact m_t dependent and $m_t \rightarrow \infty$ LO curves of Fig. 10. A blow-up of the interference region is shown on the RHS of Fig. 16 and makes this effect obvious.

On the RHS of Fig. 16, we can also see that the curve obtained by weighting the exact LO rate by $K^{m_t \rightarrow \infty}$ differs from the curve calculated using Eqs. 25,26 at the interference dip of the $m_t \rightarrow \infty$ curve. The interference dip is where the LO cross section is a minimum. Hence, the piece of the virtual contribution (Eqs. 26,31) not proportional the LO cross section makes a relatively large contribution in this region. Since the interference dip is deeper in the $m_t \rightarrow \infty$ limit (see Fig. 10), this effect is more pronounced in the $m_t \rightarrow \infty$ case. As a consequence, at the interference dip, the $m_t \rightarrow \infty$ NLO rate is not approximately proportional to the $m_t \rightarrow \infty$ LO rate. Therefore, weighting the exact LO rate by $K^{m_t \rightarrow \infty}$

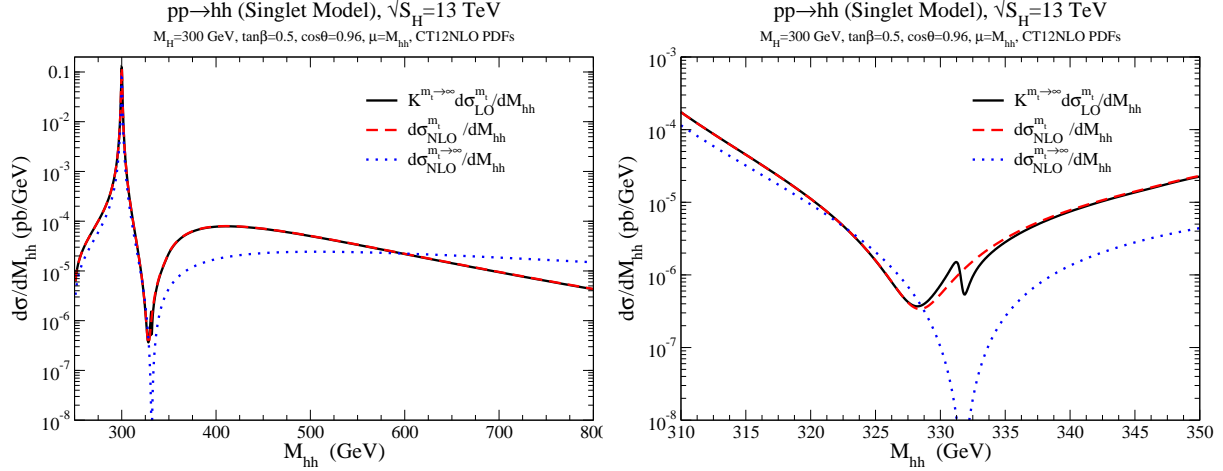


FIG. 16: NLO cross sections for $M_H = 300$ GeV and with different approximations for the top mass dependence as described in the text. The mixing parameters were set to $\tan\beta = 0.5$ and $\cos\theta = 0.96$.

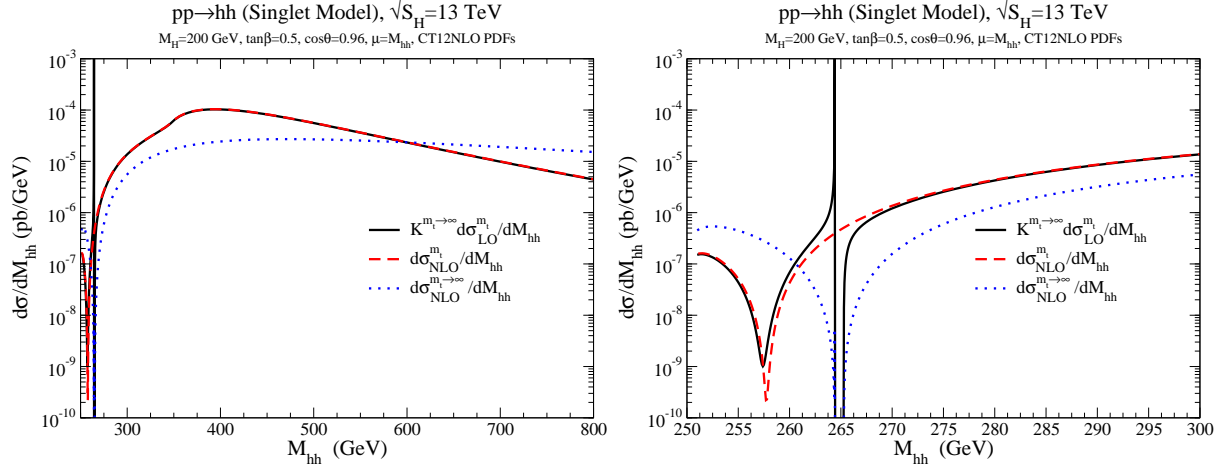


FIG. 17: NLO cross sections for $M_H = 200$ GeV and with different approximations for the top mass dependence as described in the text. The mixing parameters were set to $\tan\beta = 0.5$ and $\cos\theta = 0.96$.

does not reproduce the curves computed using Eqs. 25,26 precisely where the $m_t \rightarrow \infty$ rate has the strongest destructive interference.

It is interesting to compare with the NLO rate for a heavy Higgs mass below the threshold for a double Higgs resonance, $M_H = 200$ GeV. These results are shown in Fig. 17. In the interference region, the effects are similar, but more pronounced, to those in the $M_H = 300$ GeV case. In fact, for $M_H = 200$ GeV, the two curves computed by Eqs. 25,26 and by

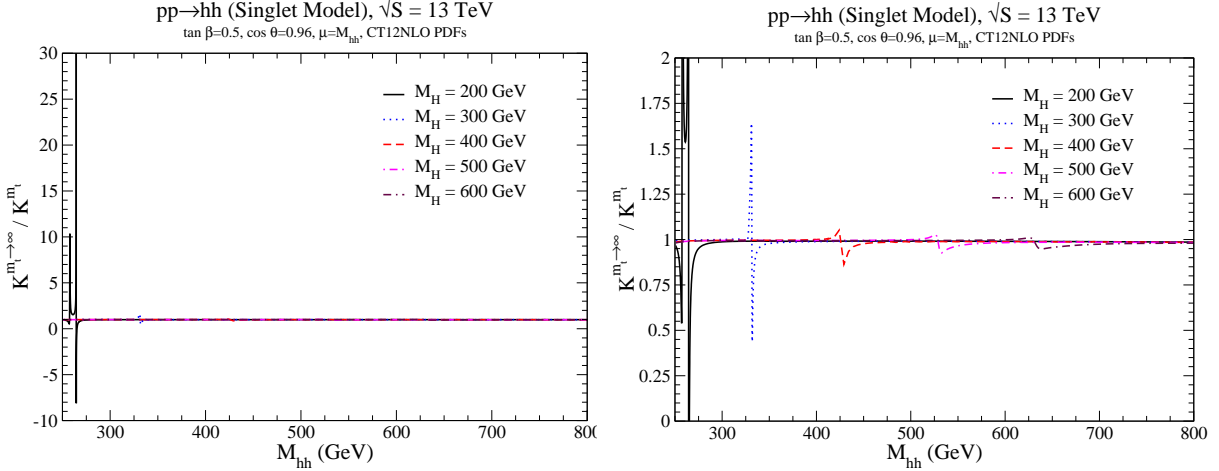


FIG. 18: Ratio of differential K-factors evaluated in the $m_t \rightarrow \infty$ limit to those calculated using the approximate m_t dependence of Eq. 25. The mixing parameters were set to $\tan \beta = 0.5$ and $\cos \theta = 0.96$.

weighting the exact LO rate by $K^{m_t \rightarrow \infty}$ do not agree at the minimum of the $\sigma_{NLO}^{m_t}$ curve in addition to the minimum of the $K^{m_t \rightarrow \infty} \sigma_{LO}^{m_t}$ curve. This can be understood by noting that as M_H increases, the interference dip of the LO cross section is more shallow (see Fig. 7). As a consequence and discussed above, as M_H increases the contribution to σ_{virt} that is not proportional to the leading order rate decreases. Hence, the curves computed using Eqs. 25,26 and weighting the exact LO rate with $K^{m_t \rightarrow \infty}$ will be in better agreement with increasing M_H . In Fig. 18 we show the ratio of the $K^{m_t \rightarrow \infty}$ and K^{m_t} (Eq. 29), which is the same as the ratio of the NLO rates calculated by weighting of the exact LO rate by $K^{m_t \rightarrow \infty}$ and using Eqs. 25,26. As can be seen, as M_H increases the two methods increasingly agree.

In Fig. 19, we show the scale dependence of the invariant mass distribution for a representative parameter point with $M_{hh}/2 < \mu < 2M_{hh}$. The LO cross sections contains exact m_t dependence and the NLO cross section is computed using Eqs. 25,26. The NLO corrections decrease the scale dependence from $\sim_{-20\%}^{+(20-30)\%}$ to $\sim \pm 15\%$. Additionally, the NLO scale dependence is fairly flat throughout the distribution; in particular, it does not appreciably change in the resonance and strong destructive interference regions.

In Fig. 20, we show the differential K-factor in the $m_t \rightarrow \infty$ limit, $K^{m_t \rightarrow \infty}$, as defined in Eq. 30. The K-factor is flat with a value of 2 – 2.2, except for spikes that occur in the regions with the strongest destructive interference. As shown in Fig. 18, the K-factor computed using Eq. 29 agrees with $K^{m_t \rightarrow \infty}$, except in the regions of strong destructive

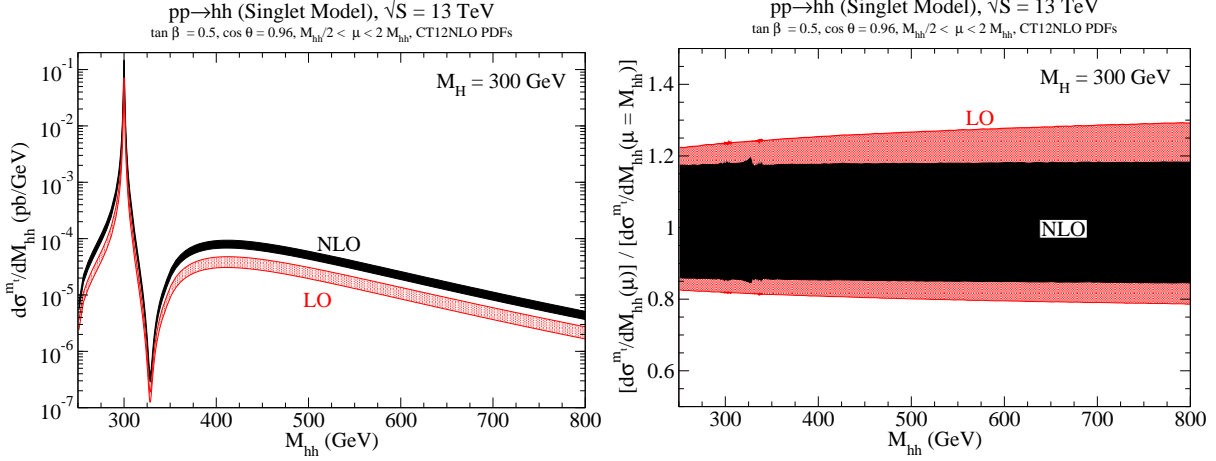


FIG. 19: Scale dependence of the invariant mass distributions for $M_H = 300$ GeV for both the NLO and LO cross sections with $M_{hh}/2 < \mu < 2M_{hh}$. The RHS shows the fractional scale dependence of the invariant mass distributions. These figures are computed using Eq. 25. The mixing parameters were set to $\tan \beta = 0.5$ and $\cos \theta = 0.96$.

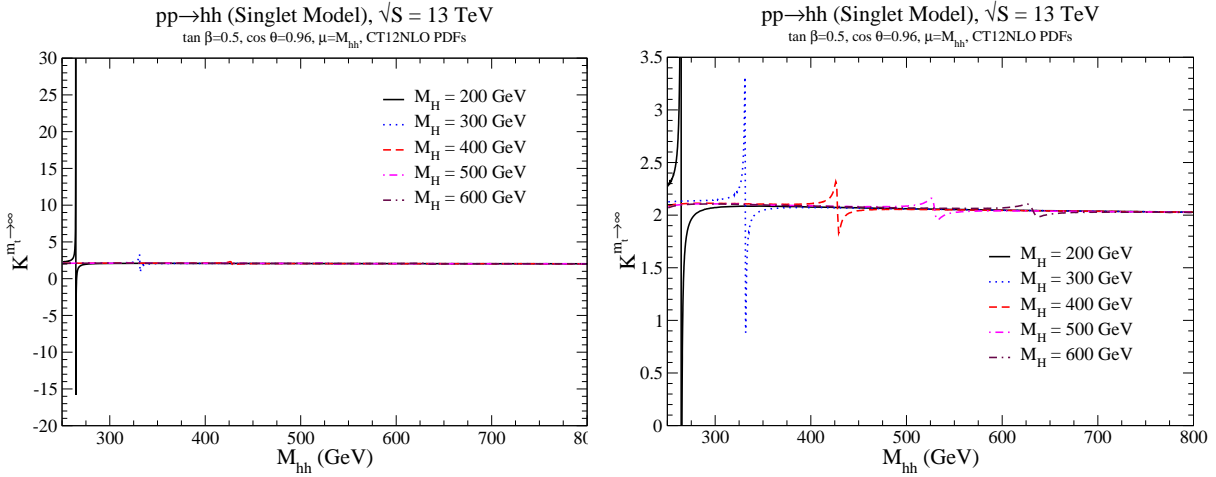


FIG. 20: $K^{m_t \rightarrow \infty}$ as defined in Eq. 29 at $\sqrt{S} = 13$ TeV for various M_H and $\tan \beta = 0.5$, $\cos \theta = 0.96$ interference.

E. Results at 100 TeV

Next we present our results for the NLO calculation of double Higgs production at $\sqrt{S} = 100$ TeV. In Fig. 21 we plot (top) $K^{m_t \rightarrow \infty}$, Eq. 30, and (bottom) the ratio of the $K^{m_t \rightarrow \infty}$ and K^{m_t} , Eq. 29. The K-factors at $\sqrt{S} = 100$ TeV are similar to those at $\sqrt{S} = 13$ TeV.

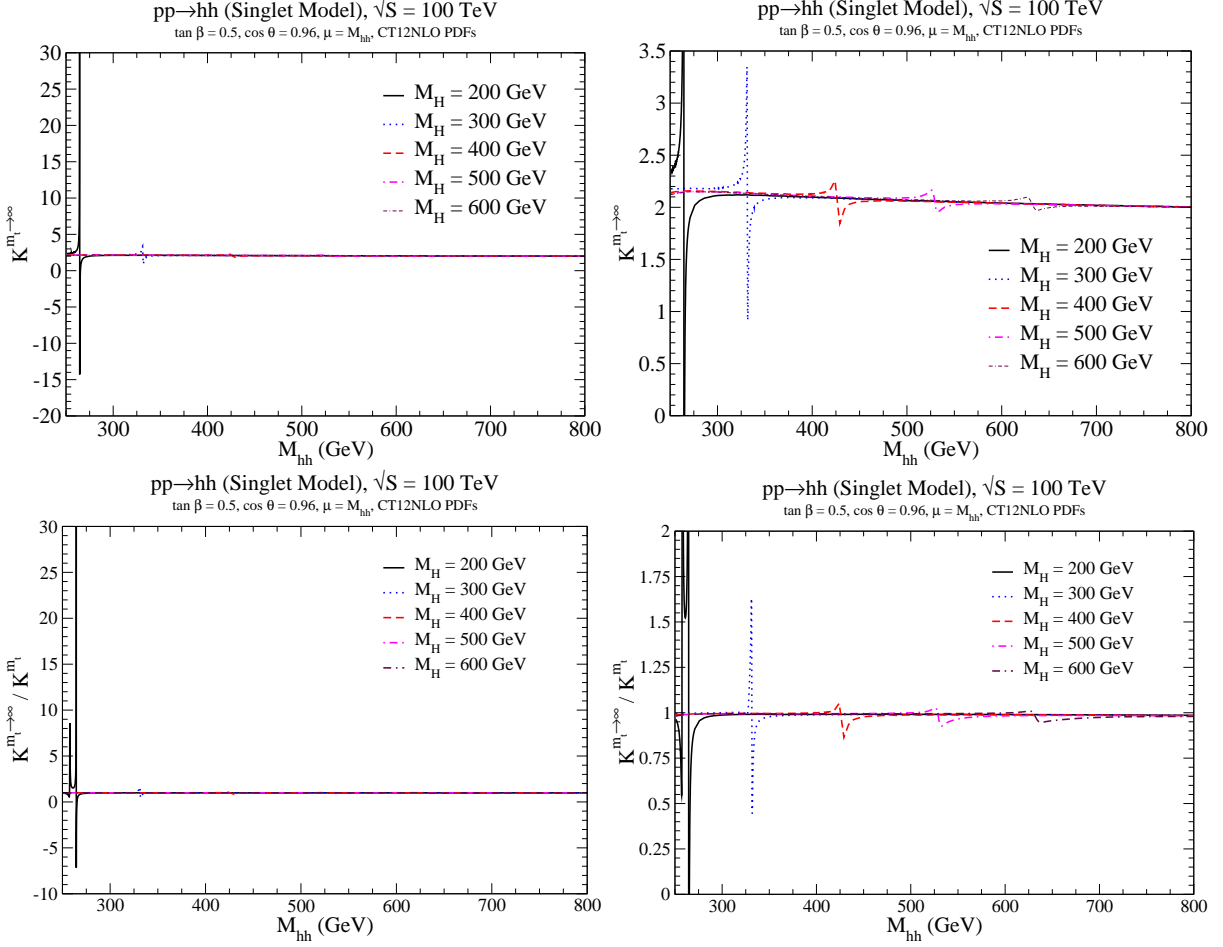


FIG. 21: (Top) $K^{m_t \rightarrow \infty}$ defined in Eq. 30. (Bottom) Ratio of $K^{m_t \rightarrow \infty}$ and K^{m_t} defined in Eq. 29. The mixing parameters were set to $\tan \beta = 0.5$ and $\cos \theta = 0.96$

Since the ratio of K-factors at 100 TeV is similar to those at 13 TeV, our comparison of the rates calculated by weighting the exact LO rate by $K^{m_t \rightarrow \infty}$ and Eqs. 25,26 will translate from the 13 TeV to 100 TeV environment.

In Fig. 22 we show the normalized invariant mass distributions at $\sqrt{S} = 13$ and 100 TeV with both $m_t \rightarrow \infty$ and the approximate finite m_t dependence of Eqs. 25,26. As noted previously, the infinite top quark mass limit overestimates the tail of the distribution. Additionally, for the SM-like contributions, the $m_t \rightarrow \infty$ limit underestimates the cross section for $M_{hh} \lesssim 550$ GeV (Fig. 4). Hence, after the strongest destructive interference, the SM-like contribution to the approximate finite m_t rate grows more quickly than in the $m_t \rightarrow \infty$ case. As a result, directly after the interference dip, the approximately finite m_t distribution grows more quickly and obtains a higher value than the $m_t \rightarrow \infty$ distribution.

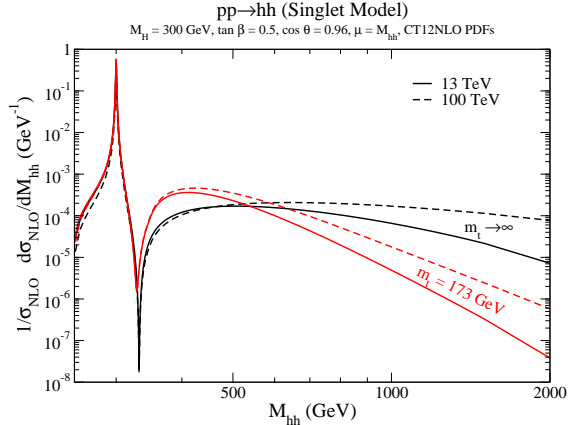


FIG. 22: Normalized invariant mass distributions for $\sqrt{S} = 13$ and 100 TeV in both the $m_t \rightarrow \infty$ limit and the approximate m_t dependence of Eq.25. The model parameters were set to $M_H = 300$ GeV, $\tan \beta = 0.5$ and $\cos \theta = 0.96$.

Finally, at $\sqrt{S} = 100$ TeV the tails of the distributions are enhanced relative to 13 TeV. This is because for a given invariant mass, the PDFs are evaluated at smaller x at 100 TeV than at 13 TeV. Hence, the enhancement of the gluon parton luminosity causes the tail of the distribution to be longer.

V. CONCLUSIONS

The production of Higgs pairs from gluon fusion is an important probe of the structure of the scalar potential. In the SM, the QCD corrections are known in an approximation where the LO rate is weighted by a K factor computed in the $m_t \rightarrow \infty$ limit, increasing both the total rate and $d\sigma/dM_{hh}$ by a factor of around 2.

We have presented results in the Higgs singlet model, where the tri-linear Higgs self coupling is modified from the SM value and significant resonant effects from the second scalar occur. The effects of the interference between the heavy scalar and SM-like contributions can be significant, altering invariant mass distributions for all M_H . For $M_H \gtrsim 450$ GeV, the interference effects can make a $\sim 10-20\%$ contribution to the total rate. For $M_H \lesssim 2m_h$, the interference effects can suppress the total cross section up to $\sim 30\%$ for a viable parameter point. Hence, in searches for heavy scalars, these effects should be included.

We compare an approximation for the NLO QCD corrections where the exact m_t dependent LO cross section is weighted by a K factor computed in the $m_t \rightarrow \infty$ limit, and

alternatively where the exact m_t dependent form factors are inserted into the NLO contributions. The approaches give similar results except in the regions with large destructive interference.

In the singlet model, the total cross section is increased by factors between 5 – 10 above the SM rate for $\tan\beta = 0.5$ and $\cos\theta = 0.96$. For larger mixing ($\tan\beta = 1$ and $\cos\theta = 0.9$), we find enhancements from the SM rate between 10 – 20 for $M_H < 500$ GeV, and the enhancement is very similar at LO and NLO. The resonant approximation to the total cross section underestimates the enhancement by about a factor of 2 at large M_H .

The singlet model demonstrates a case where the kinematic distributions of the outgoing SM Higgs pair are significantly altered from the SM, and where the higher order QCD corrections differ from those of the SM near the resonance peak.

Acknowledgements

This work is supported by the U.S. Department of Energy under grant No. DE-AC02-98CH10886 and contract DE-AC02-76SF00515. We thank Chien-Yi Chen and Tania Robens for discussions.

-
- [1] S. Profumo, M. J. Ramsey-Musolf, C. L. Wainwright, and P. Winslow, Phys. Rev. **D91**, 035018 (2015), 1407.5342.
 - [2] D. Curtin, P. Meade, and C.-T. Yu, JHEP **11**, 127 (2014), 1409.0005.
 - [3] J. R. Espinosa, T. Konstandin, and F. Riva, Nucl. Phys. **B854**, 592 (2012), 1107.5441.
 - [4] J. M. No and M. Ramsey-Musolf, Phys. Rev. **D89**, 095031 (2014), 1310.6035.
 - [5] S. Profumo, M. J. Ramsey-Musolf, and G. Shaughnessy, JHEP **08**, 010 (2007), 0705.2425.
 - [6] J. Kozaczuk, JHEP **10**, 135 (2015), 1506.04741.
 - [7] ATLAS Collaboration, CERN Report No. ATLAS-CONF-2014-010, 2014 (unpublished).
 - [8] ATLAS, G. Aad *et al.*, Phys. Rev. **D92**, 012006 (2015), 1412.2641.
 - [9] ATLAS Collaboration, CERN Report No. ATLAS-CONF-2013-030, 2013 (unpublished).
 - [10] CMS, V. Khachatryan *et al.*, JHEP **10**, 144 (2015), 1504.00936.
 - [11] ATLAS, G. Aad *et al.*, Eur. Phys. J. **C75**, 412 (2015), 1506.00285.

- [12] ATLAS, G. Aad *et al.*, Phys. Rev. Lett. **114**, 081802 (2015), 1406.5053.
- [13] CMS Collaboration, CERN Report No. CMS-PAS-HIG-13-032, 2014 (unpublished).
- [14] CMS, V. Khachatryan *et al.*, (2015), 1503.04114.
- [15] T. Robens and T. Stefaniak, Eur.Phys.J. **C75**, 104 (2015), 1501.02234.
- [16] G. M. Pruna and T. Robens, Phys.Rev. **D88**, 115012 (2013), 1303.1150.
- [17] M. Bowen, Y. Cui, and J. D. Wells, JHEP **0703**, 036 (2007), hep-ph/0701035.
- [18] M. J. Dolan, C. Englert, and M. Spannowsky, Phys. Rev. **D87**, 055002 (2013), 1210.8166.
- [19] C.-Y. Chen, S. Dawson, and I. M. Lewis, Phys. Rev. **D91**, 035015 (2015), 1410.5488.
- [20] A. Falkowski, C. Gross, and O. Lebedev, JHEP **05**, 057 (2015), 1502.01361.
- [21] D. O'Connell, M. J. Ramsey-Musolf, and M. B. Wise, Phys. Rev. **D75**, 037701 (2007), hep-ph/0611014.
- [22] V. Barger, P. Langacker, M. McCaskey, M. J. Ramsey-Musolf, and G. Shaughnessy, Phys. Rev. **D77**, 035005 (2008), 0706.4311.
- [23] C. Englert, J. Jaeckel, V. Khoze, and M. Spannowsky, JHEP **1304**, 060 (2013), 1301.4224.
- [24] C. Englert, Y. Soreq, and M. Spannowsky, JHEP **05**, 145 (2015), 1410.5440.
- [25] C. Englert *et al.*, J. Phys. **G41**, 113001 (2014), 1403.7191.
- [26] M. J. Dolan, C. Englert, N. Greiner, K. Nordstrom, and M. Spannowsky, (2015), 1506.08008.
- [27] C. Englert, F. Krauss, M. Spannowsky, and J. Thompson, Phys. Lett. **B743**, 93 (2015), 1409.8074.
- [28] D. Buttazzo, F. Sala, and A. Tesi, (2015), 1505.05488.
- [29] V. Martn Lozano, J. M. Moreno, and C. B. Park, JHEP **08**, 004 (2015), 1501.03799.
- [30] S. I. Godunov, A. N. Rozanov, M. I. Vysotsky, and E. V. Zhemchugov, (2015), 1503.01618.
- [31] T. Plehn, M. Spira, and P. Zerwas, Nucl.Phys. **B479**, 46 (1996), hep-ph/9603205.
- [32] E. N. Glover and J. van der Bij, Nucl.Phys. **B309**, 282 (1988).
- [33] S. Dawson, S. Dittmaier, and M. Spira, Phys.Rev. **D58**, 115012 (1998), hep-ph/9805244.
- [34] D. Y. Shao, C. S. Li, H. T. Li, and J. Wang, JHEP **07**, 169 (2013), 1301.1245.
- [35] D. de Florian and J. Mazzitelli, Phys.Rev.Lett. **111**, 201801 (2013), 1309.6594.
- [36] J. Grigo, K. Melnikov, and M. Steinhauser, Nucl. Phys. **B888**, 17 (2014), 1408.2422.
- [37] D. de Florian and J. Mazzitelli, (2015), 1505.07122.
- [38] R. Frederix *et al.*, Phys. Lett. **B732**, 142 (2014), 1401.7340.
- [39] J. Grigo, J. Hoff, K. Melnikov, and M. Steinhauser, PoS **RADCOR2013**, 006 (2013),

1311.7425.

- [40] J. Grigo, J. Hoff, K. Melnikov, and M. Steinhauser, Nucl.Phys. **B875**, 1 (2013), 1305.7340.
- [41] J. Baglio *et al.*, JHEP **1304**, 151 (2013), 1212.5581.
- [42] B. Hespel, D. Lopez-Val, and E. Vryonidou, JHEP **09**, 124 (2014), 1407.0281.
- [43] R. Grober, M. Muhlleitner, M. Spira, and J. Streicher, (2015), 1504.06577.
- [44] S. Dawson and W. Yan, Phys. Rev. **D79**, 095002 (2009), 0904.2005.
- [45] D. Lopez-Val and T. Robens, Phys. Rev. **D90**, 114018 (2014), 1406.1043.
- [46] S. Dawson, A. Ismail, and I. Low, Phys. Rev. **D91**, 115008 (2015), 1504.05596.
- [47] G. D. Kribs and A. Martin, Phys.Rev. **D86**, 095023 (2012), 1207.4496.
- [48] E. Asakawa, D. Harada, S. Kanemura, Y. Okada, and K. Tsumura, Phys.Rev. **D82**, 115002 (2010), 1009.4670.
- [49] C.-Y. Chen, S. Dawson, and I. Lewis, Phys.Rev. **D90**, 035016 (2014), 1406.3349.
- [50] S. Dawson, E. Furlan, and I. Lewis, Phys.Rev. **D87**, 014007 (2013), 1210.6663.
- [51] B. Batell, M. McCullough, D. Stolarski, and C. B. Verhaaren, (2015), 1508.01208.
- [52] J. Owens, A. Accardi, and W. Melnitchouk, Phys.Rev. **D87**, 094012 (2013), 1212.1702.
- [53] N. Kauer and C. O'Brien, (2015), 1502.04113.
- [54] E. Maina, JHEP **06**, 004 (2015), 1501.02139.
- [55] C.-R. Chen and I. Low, Phys. Rev. **D90**, 013018 (2014), 1405.7040.